

9Cr-1.5W-0.15Ta 耐热钢搅拌摩擦焊 焊缝组织和冲击性能分析

张超¹, 周猛兵¹, 崔雷², 陶欣¹, 王军¹, 王伟¹, 刘永长³

(1. 中国核动力研究设计院第四研究所, 成都, 610213; 2. 天津大学, 天津市现代连接技术重点实验室, 天津, 300354;
3. 天津大学, 水利安全与仿真国家重点实验室, 天津, 300354)

摘要: 对 9Cr-1.5W-0.15Ta 耐热钢搅拌摩擦焊焊缝的微观组织演变和冲击性能进行了分析. 结果表明, 由于搅拌针剧烈的机械搅拌和焊接热循环的双重作用, 搅拌摩擦焊区域内发生晶粒破碎、完全奥氏体化动态再结晶、晶界处 $M_{23}C_6$ 相溶解和晶内 M_3C 相析出, 焊后较大的冷却速率抑制晶粒长大, 促进了马氏体转变. 在 $-100 \sim 20 \text{ }^\circ\text{C}$ 温度范围内进行了冲击试验, 随着冲击试验温度的增加, 母材和 FSW 焊缝的冲击吸收能量均表现为单调增大的特征, 同时冲击断裂模式由脆性断裂逐渐转变为延性断裂. 由于 FSW 焊缝中板条马氏体的形成、“针状” M_3C 碳化物的析出, FSW 焊缝的硬度显著增大, 并且在相同温度下 FSW 焊缝的冲击韧性发生降低, 韧—脆转变温度由母材的 $-50 \text{ }^\circ\text{C}$ 升高至 $-40.2 \text{ }^\circ\text{C}$.

创新点: (1) 对厚度为 5 mm 的 9Cr-1.5W-0.15Ta 耐热钢进行搅拌摩擦焊, 分析焊缝微观组织演变特征.
(2) 获得了 9Cr-1.5W-0.15Ta 耐热钢搅拌摩擦焊焊缝的韧脆转变温度.

关键词: 9Cr-1.5W-0.15Ta 耐热钢; 搅拌摩擦焊; 微观组织; 冲击韧性; 韧—脆转变温度

中图分类号: TG 456.9 **文献标识码:** A **doi:** 10.12073/j.hjxb.20230423002

0 序言

核反应堆包层结构经受着极其恶劣的服役环境, 因此期望其在长期服役过程中保持结构和冶金完整性. 核反应堆材料主要挑战是辐照对脆化、蠕变、膨胀、开裂、氢脆以及辐照诱发产生的缺陷等影响. 9Cr-1.5W-0.15Ta 耐热钢具有较低的辐照肿胀系数和热膨胀系数、良好的韧性、高蠕变强度、高抗氧化性和较高的导热性等优异的热物理、力学性能^[1-3], 被认为是核反应堆包壳结构的理想候选材料之一, 如铅铋反应堆、钠冷快堆等^[4-5]. 近年来, 研究人员提出用固态连接方法—搅拌摩擦焊 (friction stir welding, FSW) 实现钢铁材料的连接, 由于其焊接热输入和焊接峰值温度较低, 焊接变形和残余应力较小, 同时实现了焊缝微观组织的细化, 使焊缝性能与母材接近^[6-7].

韧—脆转变温度 (ductile-brittle transition temperature, DBTT) 代表金属材料断裂从高能塑性弯曲/变形 (延性) 变为低能量破碎 (脆性) 的温度点. 在较高温度下, 金属材料具有较高的延展性和较低的强度; 而在较低的温度下, 材料强度较大, 且断裂模式也从韧性断裂变为脆性断裂^[8]. 在晶体结构为体心立方和密排六方的材料中可以观察到明显的 DBTT. 已有研究表明^[9-10], 9Cr-1.5W-0.15Ta 耐热钢为体心立方晶体结构, 一般情况下其 DBTT 低于 $-50 \text{ }^\circ\text{C}$. 在 FSW 过程中, 焊缝区域受到焊接热循环和搅拌针的机械作用, 导致晶粒细化、马氏体转变和 $M_{23}C_6$ 碳化物溶解的发生^[11], 并且微观组织的变化必然会影响力学性能^[12-13].

文中以 9Cr-1.5W-0.15Ta 耐热钢和其 FSW 焊缝为研究对象, 研究 FSW 焊缝微观组织演变、冲击韧性以及韧—脆转变温度, 分析 9Cr-1.5W-0.15Ta 耐热钢和其 FSW 焊缝微观组织与冲击韧性、韧—脆转变温度之间的联系, 并阐明了冲击断裂失效机制, 为优化焊接工艺和 FSW 焊接接头组织和性能提供重要依据.

1 试验方法

试验所用母材 (base metal, BM) 为 9Cr-1.5W-0.15Ta 耐热钢, 其具体的化学成分如表 1 所示, 焊接试板厚度为 5 mm. 母材的热处理工艺为 1 000 °C 正火处理 60 min, 水淬, 然后在 700 °C 回火 60

min. FSW 试验是在型号为 FSW-3LM-020 焊接设备进行的, 使用的搅拌工具由 W-25%Re 合金制成, 其搅拌针形状为带螺纹的圆锥形, 搅拌针长度为 4.7 mm, 搅拌针半径逐渐从 6.0 mm 变至 2.8 mm, 轴肩尺寸为 18 mm. 焊接工艺参数为焊接速度 60 mm/min, 焊接转速 300 r/min, 焊接压力 10 kN, 轴肩下压量为 0.1 mm, 焊接后焊缝的宏观形貌如图 1 所示.

表 1 9Cr-1.5W-0.15Ta 耐热钢化学成分 (质量分数, %)

Table 1 Chemical composition of the 9Cr-1.5W-0.15Ta heat resistant steel

C	Cr	Mn	V	W	Ta	Si	Zr	N	S和P	Fe
0.1	9	0.5	0.2	1.5	0.15	0.05	0.005	0.007	0.002	余量

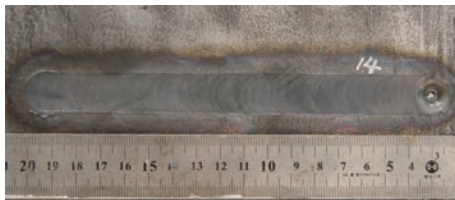


图 1 FSW 焊缝的宏观形貌

Fig. 1 Macromorphology of FSW weld

冲击试样尺寸和加工符合 ASTM:A370-10 金属性能评定方法要求, 并对焊缝表面和背面进行机械加工至光滑, 试样尺寸如图 2 所示 (V 形缺口位于焊缝横截面的中间, 深度为 2 mm, 底部曲率半径为 0.25 mm, 夹角为 45°). 参照国家标准 GB/T 229—2007 《金属材料-夏比摆锤冲击试验方法》进行冲击试验, 冲击试验温度为 -100 ~ 20 °C, 在相应的温度下保温 10 ~ 15 min, 每组试验测试 3 个试样, 取 3 个测试值的平均值作为试验值, 试验设备是摆锤式冲击试验机, 硬度试验是在金相试样的焊缝区域测试, 载荷为 9.8 N, 加载时间为 15 s.

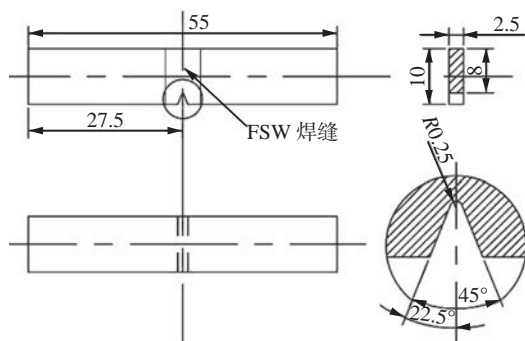


图 2 V 形缺口冲击试样尺寸 (mm)

Fig. 2 Dimensions of V-notch impact specimen

为了进行微观组织观察, 沿垂直于焊接方向切

取尺寸为 25 mm × 10 mm 的试样, 经过粗磨、细磨和抛光后, 在 5 g FeCl₃, 20 mL 盐酸和 100 mL 蒸馏水的腐蚀液中侵蚀 90 s 制备金相试样. 采用型号为 OLYMPUS GX51 光学显微镜和型号为 JEOL-F7800 热场发射电子扫描显微镜 (SEM) 对接头区域微观组织特征进行观察分析. 采用型号为 Tecnai G2F30 透射电子显微镜在 300 kV 加速电压下分析析出相特征, 同时进行能谱测试 (EDS), 以分析第二相类型和组成.

2 试验结果与分析

2.1 微观组织分析

图 3 为母材和 FSW 焊缝的微观组织特征. 由图 3(a) 可以看出, 经过一系列热处理后, 9Cr-1.5W-0.15Ta 耐热钢母材表现为完全的回火组织特征. 在较大的放大倍数下的 SEM 观察可以发现, 母材主要由回火板条马氏体、块状铁素体、“片状”残余奥氏体 (firkm-like retained austenite, Firkm-like RA) 和大量的析出相组成, 如图 3(a) ~ 图 3(d) 所示, 原奥氏体晶粒尺寸大约为 ~ 20 μm, 如图 3(a) 和图 3(b) 所示. FSW 焊缝微观组织主要由板条马氏体组成, 晶粒尺寸发生明显细化, 平均晶粒尺寸为 ~ 5 μm, 如图 3(e) 和图 3(f) 所示, 这是由于 FSW 焊缝区域受到搅拌针剧烈的机械搅拌和焊接热循环的双重作用, 导致搅拌针附近的材料焊接过程中发生了严重的塑性变形, 进而导致晶粒破碎和完全奥氏体动态再结晶的发生, 有利于焊缝晶粒细化, 并且焊后经历较大的冷却速率, 抑制焊缝晶粒长大, 促进焊缝内马氏体转变^[14], 因此母材的原始回火组织

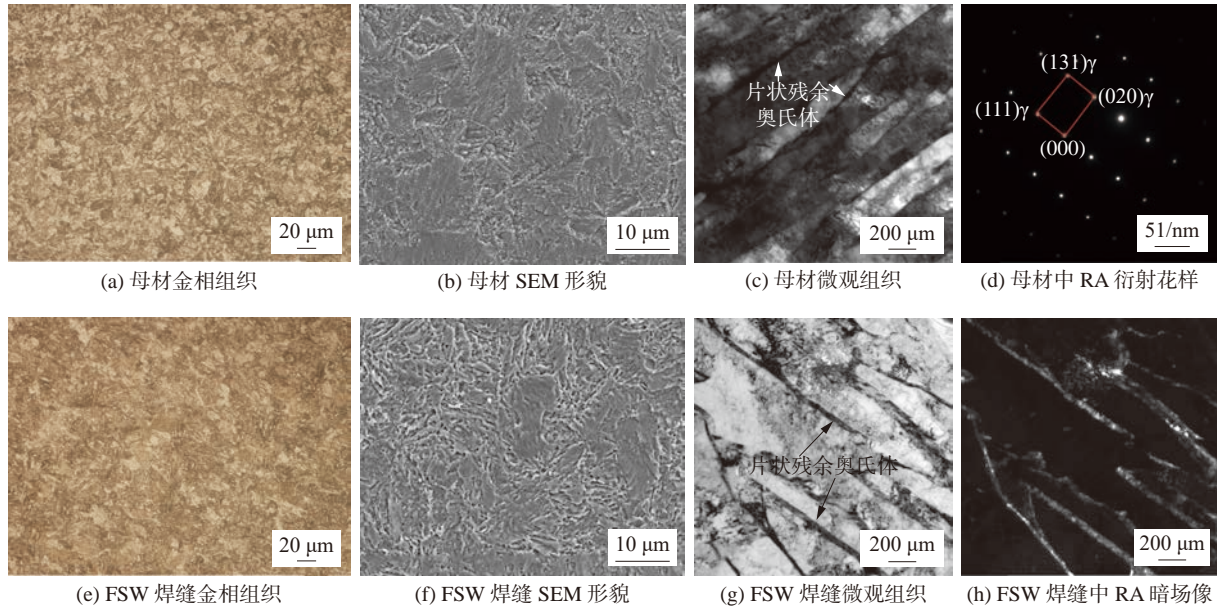


图 3 母材和 FSW 焊缝的微观组织特征

Fig. 3 Microstructure characteristics of BM and FSW weld. (a) the metallographic structure of BM; (b) the morphology of BM; (c) the microstructure of BM; (d) the RA diffraction patterns in BM; (e) the metallographic structure of FSW weld; (f) the morphology of FSW weld; (g) the microstructure of FSW weld; (h) the RA dark field image in FSW

FSW 后焊缝区域转变为细小的板条马氏体组织。此外,在 TEM 下观察可以发现,马氏体板条之间存在 Fikm-like RA 组织,马氏体板条平均宽度为 ~300 nm,如图 3(g)和图 3(h)所示。

图 4 为母材和 FSW 焊缝的析出相分布特征。如图 4(a)所示,在母材中沿原奥氏体晶界 (prior

austenite grain boundaries, PAGBs) 和板条界处分布着大量的 $M_{23}C_6$ (M: Cr, Fe, W, Mn) 类型的碳化物,表现为“棒状”和“球状”的形态特征,而细小的“球状”MX (M: Ta, V, X: C, N) 类型的析出相则趋向于马氏体板条内部 (图 4(c)),与前期相关研究报道结果一致^[11]。然而 FSW 后,焊缝区域内沿 PAGBs 和

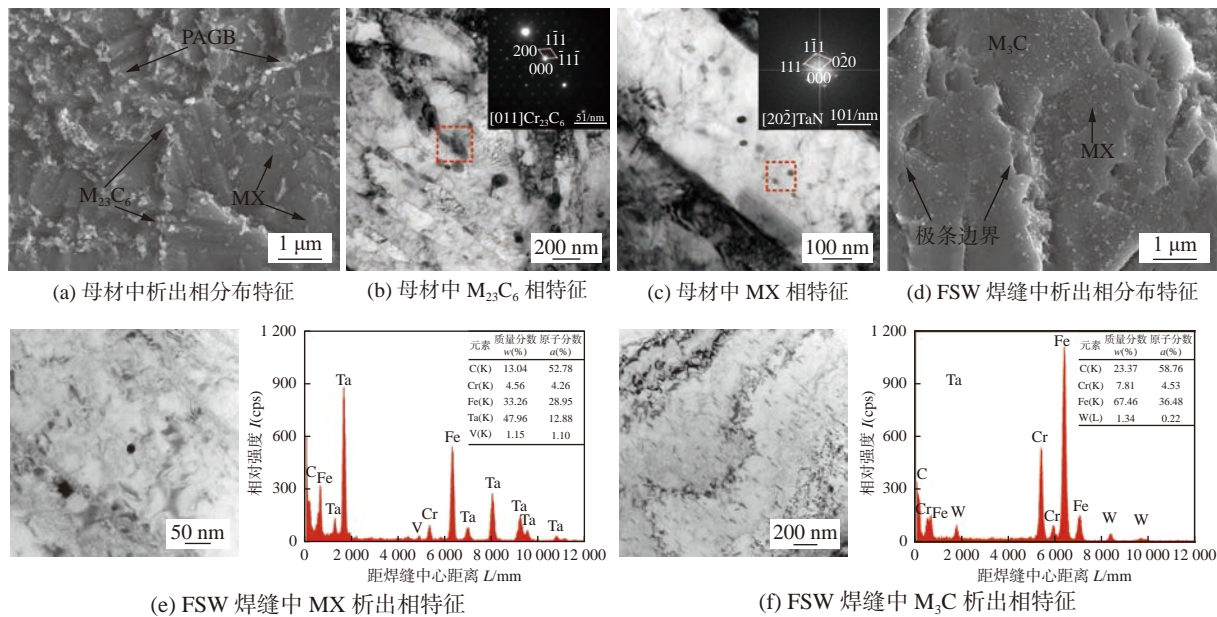


图 4 母材和 FSW 焊缝的析出相分布特征

Fig. 4 Precipitates characteristics of BM and FSW weld. (a) the distribution characteristics of precipitated phases in the BM; (b) the characteristics of $M_{23}C_6$ phase in the BM; (c) the characteristics of MX phase in the BM; (d) the distribution characteristics of precipitated phases in the FSW weld; (e) the characteristics of MX phase in the FSW weld; (f) the characteristics of M_3C phase in the FSW weld

马氏体板条界没有发现 $M_{23}C_6$ 类型的碳化物,在马氏体板条内部分布着大量的“球状”MX 和“针状” M_3C (M: Fe, Cr) 析出相(图 4(d)、图 4(e)和图 4(f)),这表明 FSW 促进晶界处的 $M_{23}C_6$ 碳化物的溶解和 M_3C 碳化物的析出;而对 MX 碳氮化物无明显影响,这与 FSW 焊缝经历的焊接热循环有关,即峰值温度高于 $M_{23}C_6$ 碳化物的溶解温度($\sim 850\text{ }^\circ\text{C}$),而远低于 MX 相的熔点^[15-17].

2.2 力学性能分析

2.2.1 硬度试验

9Cr-1.5W-0.15Ta 耐热钢的硬度值为 272 HV,而 FSW 焊缝的硬度发生明显增大,其硬度值为 425 HV,即焊缝区发生明显硬化,这主要是由于在焊接过程中焊接热循环峰值温度高于母材的相变温度($\geq A_{c3}$),在焊后快速冷却后焊缝中形成了大量的板条状马氏体组织,导致焊缝的硬度增大.

2.2.2 冲击韧性及脆性转变温度

在 $-100\sim 20\text{ }^\circ\text{C}$ 的温度内采用夏比 V 形缺口试样进行冲击试验,如图 2 所示,冲击试验结果统计如表 2 所示,9Cr-1.5W-0.15Ta 耐热钢和 FSW 焊缝冲击韧性随试验温度的变化曲线如图 5 所示.与母材相比,FSW 焊缝在 $-100\sim 20\text{ }^\circ\text{C}$ 的温度内的冲击韧性均发生了下降.当试验温度低于 $-35\text{ }^\circ\text{C}$ 时,可以观察到过渡转变温度范围,即随着试验温度降低,冲击断裂模式从韧性断裂逐渐变为脆性断裂.文中对于 DBTT 的估算是基于 85 J/cm^2 冲击韧性标准的^[18].由图 5 可知,母材的 DBTT 为 $-50\text{ }^\circ\text{C}$,而 FSW 焊缝的 DBTT 则增加至 $-40.2\text{ }^\circ\text{C}$,同时焊缝区域内的微观组织演变也导致了上平台能量(USE)的降低.

表 2 母材和 FSW 焊缝冲击试验结果
Table 2 Impact test results of the base materials and FSW welds

温度 $T/^\circ\text{C}$	母材平均冲击 吸收功能量 $A_{KVb}/(\text{J}\cdot\text{cm}^{-2})$	FSW 焊缝平均 冲击吸收能量 $A_{KVw}/(\text{J}\cdot\text{cm}^{-2})$
20	155.1	132.7
0	149.7	122.0
-20	130.1	107.5
-40	96.1	85.8
-60	69.1	58.5
-80	45.0	33.7
-100	21.4	12.9

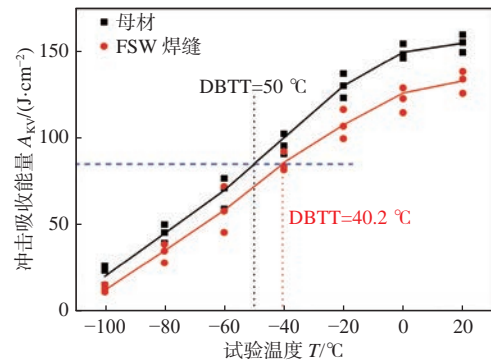


图 5 母材和 FSW 焊缝冲击韧性随试验温度的变化曲线
Fig. 5 Transformation curve of impact toughness of base metal and FSW weld with test temperature

与母材相比,FSW 焊缝的晶粒尺寸发生明显细化,但母材的冲击韧性仍然高于 FSW 焊缝的冲击韧性,这主要与 FSW 过程中板条马氏体转变、位错增殖和针状第二相析出等因素有关.首先,板条马氏体转变造成局部的应力集中,并且马氏体硬度较大,不利于应力释放,因此在冲击变形过程中促进显微裂纹形核^[19];其次,FSW 过程涉及较大的塑性变形,促进了位错增殖,导致位错缠结密度增加,抑制了位错的运动,导致应力集中和应力松弛,从而促进了显微裂纹的形成^[20-21];最后,“针状”的 M_3C 碳化物的析出也增加了显微裂纹形核的可能.

2.2.3 冲击断口形貌

图 6 为母材在不同温度下的冲击断口形貌.图 6(a)~图 6(c)为母材在 $20\sim -20\text{ }^\circ\text{C}$ 的冲击断口形貌,主要表现为纤维状韧窝特征,同时在晶界存在少量的撕裂痕,但随着试验温度的升高,撕裂痕和解理面逐渐消失,断裂方式属于微孔聚集型断裂.当试验温度降低至 $-40\text{ }^\circ\text{C}$ 时,如图 6(d)所示,冲击断口形貌中韧窝密度相对减少,也可以发现一些河流花样和解理面.在 $-60\sim -80\text{ }^\circ\text{C}$ 温度下母材冲击断裂的断口形貌分别如图 6(e)和图 6(f)所示,表现为完全的河流花样和解理台阶特征,这表明在低于 $-60\text{ }^\circ\text{C}$ 时母材为脆性断裂失效机理.

图 7 为 FSW 焊缝在 $-80\sim 20\text{ }^\circ\text{C}$ 温度的冲击断口形貌.如图 7(a)~图 7(c)所示,随着冲击试验温度的下降,冲击断口内逐渐出现少量撕裂痕,这是由于随着温度的降低,塑性变形能力在冲击变形过程逐渐变弱,导致其冲击韧性恶化.在 $-20\text{ }^\circ\text{C}$ 温度下的冲击断口形貌表现为大小形状均匀的韧窝特征,在部分韧窝底部存在第二相粒子脱落的现象,并且由于冲击变形被限制而形成少量的撕裂痕,即

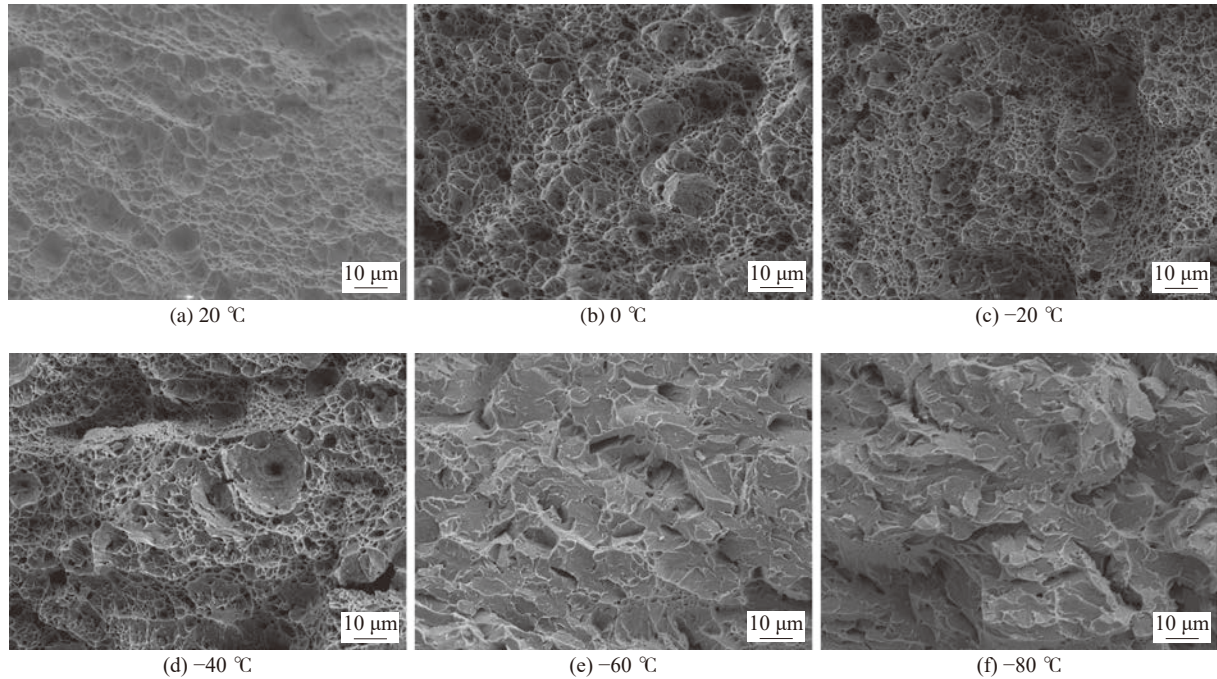


图6 母材在不同温度下的冲击断口形貌

Fig. 6 Impact fracture morphology of BM under different temperature. (a) 20 °C; (b) 0 °C; (c) -20 °C; (d) -40 °C; (e) -60 °C; (f) -80 °C

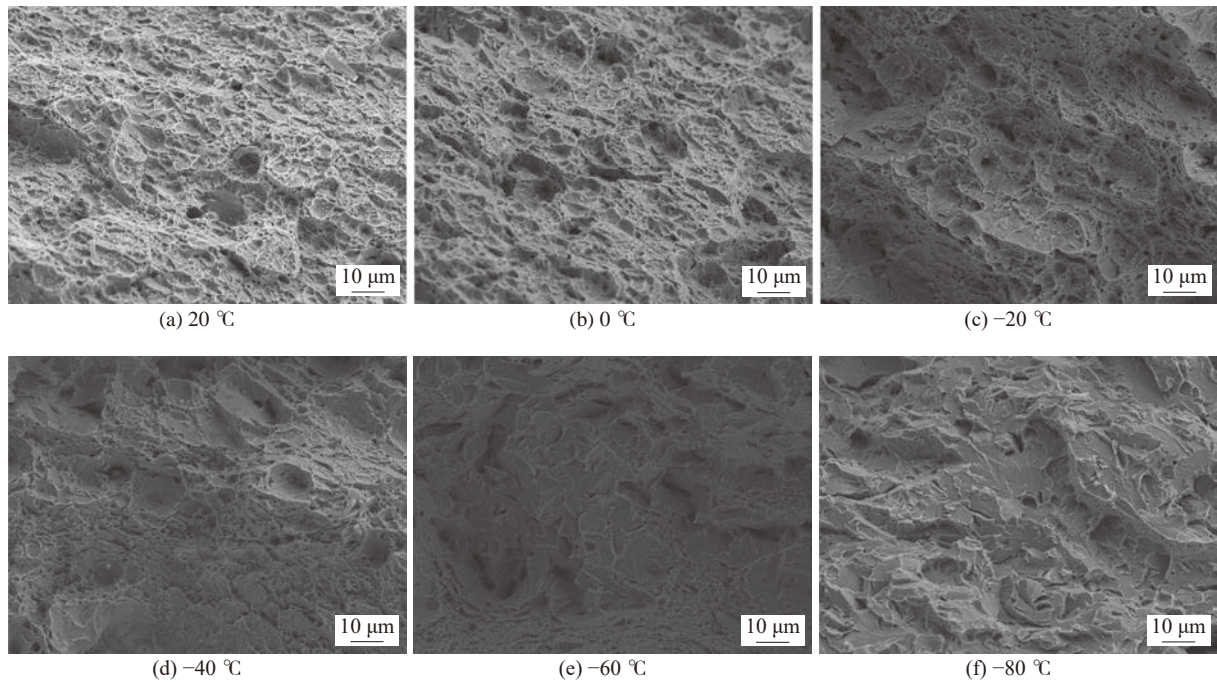


图7 FSW焊缝在不同温度下的冲击断口形貌

Fig. 7 Impact fracture morphology of FSW welds under different temperature. (a) 20 °C; (b) 0 °C; (c) -20 °C; (d) -40 °C; (e) -60 °C; (f) -80 °C

表明断裂方式属于微孔聚集型断裂;在-40 °C 温度下冲击断裂后的断口形貌如图 7(d) 所示,可以容易地发现解理面和韧窝结构,这表明该温度可能为韧-脆转变的过渡温度范围;如图 7(e)~图 7(f) 所示,FSW 焊缝在冲击试验温度低于-60 °C 冲击断裂后,冲击断口形貌主要表现为河流花样、撕开裂纹

和撕裂痕等脆性断裂特征,且无颈缩现象,即表明断裂模式属于准解理断裂。

3 结论

(1) 9Cr-1.5W-0.15Ta 耐热钢母材主要由回火

马氏体组成,同时在晶界上和晶内分别分布有大量的 $M_{23}C_6$ 碳化物和细小的 MX 析出相;FSW 后,焊缝内发生晶粒细化和板条马氏体转变,晶界处的 $M_{23}C_6$ 碳化物完全溶解,伴随着有“针状” M_3C 碳化物在晶内析出。

(2) 由于 FSW 焊缝中大量板条马氏体生成、位错增值以及“针状” M_3C 碳化物析出,导致焊缝的冲击韧性降低,在相同试验温度下,FSW 焊缝冲击韧性发生降低,相应地 9Cr-1.5W-0.15Ta 耐热钢经 FSW 焊接后,其 DBTT 从 $-50\text{ }^\circ\text{C}$ 升高至 $-40.2\text{ }^\circ\text{C}$ 。

(3) 对于母材和 FSW 焊缝,当冲击试验温度降低至各自的 DBTT 以下时,冲击断口形貌表现为脆性断裂特征;当冲击试验温度处于各自的 DBTT 附近时,以延性和脆性混合模式断裂;在高于各自的 DBTT 的温度下冲击时,冲击断口表现为典型的韧窝特征,即以延性模式断裂。

参考文献

- [1] Byun T S, Yoon J H, Hoelzer D T, *et al.* Process development for 9Cr nanostructured ferritic alloy (NFA) with high fracture toughness[J]. *Journal of Nuclear Materials*, 2014, 449: 290 – 299.
- [2] 李萍, 丁方强, 薛可敏. 低活化马氏体钢真空扩散焊接工艺[J]. *焊接学报*, 2018, 39(1): 93 – 96.
Li Ping, Ding Fangqiang, Xue Kemin. Vacuum diffusion welding process of low activation martensite steel[J]. *Transactions of the China Welding Institution*, 2018, 39(1): 93 – 96.
- [3] 周军, 邱绍宇, 邱日盛, 等. Si 含量对 9%Cr 铁素体马氏体钢 Laves 相析出行为和冲击性能的影响[J]. *材料热处理学报*, 2022, 43(5): 116 – 123.
Zhou Jun, Qiu Shaoyu, Qiu Risheng, *et al.* Effect of Si content on laves phase precipitation behavior and impact properties of 9% Cr ferritic martensitic steel[J]. *Journal of Material Heat Treatment*, 2022, 43(5): 116 – 123.
- [4] Dudko V, Belyakov A, Kaibyshev R. Origin of threshold stresses in a P92-type steel[J]. *Transactions of the Indian Institute of Metals*, 2016, 69: 223 – 227.
- [5] Chatterjee A, Moitra A, Bhaduri A K, *et al.* Dynamic fracture behaviour of thermo-mechanically processed modified 9Cr-1Mo steel[J]. *Engineering Fracture Mechanics*, 2016, 149: 74 – 88.
- [6] 唐文坤, 杨新歧, 李胜利, 等. 焊接参数对铁素体不锈钢搅拌摩擦焊接头组织及性能的影响[J]. *材料工程*, 2019, 47(5): 115 – 121.
Tang Wenshen, Yang Xinqi, Li Shengli, *et al.* Effect of welding parameters on microstructure and properties of friction stir welded joints of ferritic stainless steel[J]. *Journal of Materials Engineering*, 2019, 47(5): 115 – 121.
- [7] 邓运来, 邓舒浩, 叶凌英, 等. 焊后热处理对 AA7204-T4 铝合金搅拌摩擦焊接头组织与力学性能的影响[J]. *材料工程*, 2020, 48(4): 131 – 138.
Deng Yunlai, Deng Shuhao, Ye Lingying, *et al.* Effect of post weld heat treatment on microstructure and mechanical properties of AA7204-T4 aluminum alloy friction stir welded joint[J]. *Journal of Materials Engineering*, 2020, 48(4): 131 – 138.
- [8] 宋婕, 常英珂, 吴瑞德, 等. 13Cr11Ni2W2MoV 马氏体热强不锈钢的韧-脆转变及脆化机理[J]. *材料导报*, 2022, 4: 164 – 168.
Song Jie, Chang Yingke, Wu Ruide, *et al.* Ductile brittle transition and embrittlement mechanism of 13Cr11Ni2W2MoV martensitic heat strength stainless steel[J]. *Materials Review*, 2022, 4: 164 – 168.
- [9] Zhang Chao, Cui Lei, Wang Dongpo, *et al.* Effect of microstructures to tensile and impact properties of stir zone on 9%Cr reduced activation ferritic/martensitic steel friction stir welds[J]. *Materials Science and Engineering A*, 2018, 729: 257 – 267.
- [10] Tavassoli A A F, Diegele E, Lindau R, *et al.* Current status and recent research achievements in ferritic/martensitic steels[J]. *Journal of Nuclear Materials*, 2014, 455: 269 – 276.
- [11] Zhang C, Cui L, Liu Y, *et al.* Microstructures and mechanical properties of friction stir welds on 9% Cr reduced activation ferritic/martensitic steel[J]. *Journal of Materials Science & Technology*, 2018, 34: 756 – 766.
- [12] Chatterjee A, Chakrabarti D, Moitra A, *et al.* Effect of normalization temperatures on ductile-brittle transition temperature of a modified 9Cr-1Mo steel[J]. *Materials Science & Engineering A*, 2014, 618: 219 – 231.
- [13] Zhao M, Zeng T, Li J, *et al.* Identification of the effective grain size responsible for the ductile to brittle transition temperature for steel with an ultrafine grain size ferrite/cementite microstructure with a bimodal ferrite grain size distribution[J]. *Materials Science & Engineering A*, 2011, 528: 4217 – 4221.
- [14] Chatterjee A, Chakrabarti D, Moitra A, *et al.* Effect of deformation temperature on the ductile-brittle transition behavior of a modified 9Cr-1Mo steel[J]. *Materials Science and Engineering A*, 2015, 630: 58 – 70.
- [15] Noh S, Ando M, Tanigawa H, *et al.* Friction stir welding of F82H steel for fusion applications[J]. *Journal of Nuclear Materials*, 2016, 478: 1 – 6.
- [16] Sawada K, Hara T, Tabuchi M, *et al.* Microstructure characterization of heat affected zone after welding in Mod. 9Cr-1Mo steel[J]. *Materials Characterization*, 2015, 101: 106 – 113.
- [17] Pandey C, Giri A, Mahapatra M M. Evolution of phases in P91 steel in various heat treatment conditions and their effect on microstructure stability and mechanical properties[J]. *Materials Science and Engineering:A*, 2016, 664: 58 – 74.
- [18] American Society of Testing Materials. Standard methods for

- notch bar impact testing of metallic materials: ASTM E23 [S]. West Conshohocken, Pa: ASTM International, 2013.
- [19] Zhang J C, Di H S, Deng Y G, *et al.* Effect of martensite morphology and volume fraction on strain hardening and fracture behavior of martensite–ferrite dual phase steel[J]. *Materials Science and Engineering A*, 2015, 627: 230 – 240.
- [20] 赵洋洋, 林可欣, 王颖, 等. 基于位错模型的增材制造构件疲劳裂纹萌生行为 [J]. *焊接学报*, 2023, 44(7): 1 – 8.
Zhao Yangyang, Lin Kexin, Wang Ying, *et al.* Fatigue crack initiation behavior of additive manufacturing components based on dislocation model[J]. *Transactions of the China Welding Institution*, 2023, 44(7): 1 – 8.
- [21] 田成川, 赵海, 田妮, 等. 长期服役对 P91 钢蒸汽管道接头疲劳裂纹扩展行为的影响 [J]. *材料与冶金学报*, 2023, 22(6): 588 – 594.
Tian Chengchuan, Zhao Hai, Tian Ni, *et al.* Effect of long-term service on fatigue crack propagation behavior of P91 steel steam pipe joint[J]. *Journal of Materials and Metallurgy*, 2023, 22(6): 588 – 594.

第一作者:张超, 硕士; 主要从事低活化铁素体/马氏体钢、耐热钢搅拌摩擦焊连接机理、铝合金高能束焊接技术以及固相连接技术的相关研究工作; Email: 569405731@qq.com.

(编辑: 郑红)

[上接第 35 页]

- [18] Li C, Wang Q, Jiao W, *et al.* Deep learning-based detection of penetration from weld pool reflection images[J]. *Welding Journal*, 2020, 99(9): 239s – 245s.
- [19] Liu Z, Lin Y, Cao Y, *et al.* Swin transformer: Hierarchical vision transformer using shifted windows[C]//Proceedings of the IEEE/CVF International Conference on Computer Vision. 2021: 10012 – 10022.
- [20] Liang S J, Yu M X, Lu W S, *et al.* A lightweight vision transformer with symmetric modules for vision tasks[J]. *Intelligent Data Analysis*, 2023, 27(6): 1741 – 1757.
- [21] Yuan K, Guo S, Liu Z, *et al.* Incorporating convolution designs into visual transformers[C]//Proceedings of the IEEE/CVF International Conference on Computer Vision (ICCV), 2021: 559 – 568.
- [22] Howard A, Sandler M, Chu G, *et al.* Searching for mobilenetv3[C]//Proceedings of the IEEE/CVF International Conference on Computer Vision, 2019: 1314-1324.

第一作者:王颖, 硕士, 副教授; 主要研究方向为智能焊接、先进机器人工程、深度学习、人工智能等; Email: nepu_wy@163.com.

(编辑: 郑红)

information contained in the class labels; and lastly, the fusion of the underlying features and the high-level semantic features in the LeFF module improves the model's ability to represent the features of the melt pool. Simulation experiments show that the proposed model obtains higher accuracy and faster detection speed compared with MobileNetV3, ResNet50, ShuffleNetV2, DeiT, and CeiT models.

Highlights: A GTAW weld fusion state identification model based on improved CeiT is developed, which obtains higher accuracy and faster detection speed compared with other models.

Key words: image processing; melt pool; penetration state; CeiT network; gas tungsten arc welding

Microstructure and impact properties for friction stir welds of 9Cr-1.5W-0.15Ta heat resistant steel ZHANG Chao¹, ZHOU Mengbing¹, CUI Lei², TAO Xin¹, WANG Jun¹, WANG Wei¹, LIU Yongchang³(1. Fourth Institute of Nuclear Power Institute of China, Chengdu, 610213, China; 2. Tianjin Key Laboratory of Advanced Joining Technology, Tianjin University, Tianjin, 300354, China; 3. State Key Lab of Hydraulic Engineering Simulation and Safety, Tianjin University, Tianjin, 300354, China). pp 36-42

Abstract: In this paper, the microstructure evolution and impact properties of friction stir welds of 9Cr-1.5W-0.15Ta heat resistant steel were studied. The results showed that due to the double effects of the mechanical stirring of the stir tool and the welding thermal cycle, grain breaking, fully austenitized dynamic recrystallization, dissolution of $M_{23}C_6$ phase at the grain boundaries and formation of M_3C are materialized in the welds. Higher cooling rate after welding restrains the growth of grains, and promotes martensite transformation. The impact test was conducted in the temperature range of $-100 \sim 20$ °C. With the increase of impact test temperature, the impact absorbing energy of base metal and FSW weld metal is monotonously increased, and the impact fracture mode changes from brittle fracture to ductile fracture. Due to the formation of lath martensite and the precipitation of "acicular" M_3C carbide in FSW weld, the hardness of FSW weld increases significantly. At the same temperature, the impact toughness of FSW weld decreases. And, the ductile-brittle transition temperature of FSW weld increases from -50 °C of the base metal to -40.2 °C.

Highlights: (1) The friction stir welding on 9Cr-1.5W-0.15Ta heat resistant steel with a thickness of 5 mm is per-

formed, and the microstructure evolution characteristics of the weld is analyzed.

(2) The ductile-brittle transition temperature for FSW weld of 9Cr-1.5W-0.15Ta heat resistant steel is obtained.

Key words: 9Cr-1.5W-0.15Ta heat resistant steel; friction stir welding; microstructure; impact toughness; ductile-brittle transition temperature

Effect of wire feeding angle and wire feeding mode on the formation of single-track laser wire deposition layer

YANG Xin¹, HAN Hongbiao^{1,2,3}, YAN Chenxiao¹, WANG Rui¹(1. Henan University of Science and Technology, Luoyang, 471003, China; 2. Henan Key Laboratory for Machinery Design and Transmission System, Luoyang, 471003, China; 3. Longmen Laboratory, Luoyang, 471003, China). pp 43-48,56

Abstract: In order to study the influence of the direction of the welding wire into the molten pool on the formation of the deposited layer during the laser additive manufacturing by paraxial wire feeding, single-track laser wire deposition tests were carried out under different wire feeding angles and wire feeding modes. The variation of layer width, layer height, surface roughness, cross-sectional morphology and substrate fusion depth of deposited layer with wire feeding angle and wire feeding mode was analyzed. The results show that the wire feeding angle and wire feeding mode of paraxial wire feeding influence the formation of single-track laser deposited layer, and the effect of wire feeding mode on the size and shape of deposited layer is greater than that of wire feeding angle. With the increase of wire feeding angle, all the substrate fusion depth decreases gradually, the layer width of front feeding and back feeding decreases gradually, the layer height of deposited layer increases gradually, however, the layer width, layer height and surface roughness of side feeding change little. The cross-section shape of front feeding and back feeding deposited layer is symmetrical and circular, while the cross-section shape of side feeding deposited layer is asymmetrical and the highest point is biased towards the wire side. The layer width and substrate fusion depth of front feeding are larger and the layer height is smaller, while the layer width and substrate fusion depth of the back feeding are smaller and the layer height is larger.

Highlights: (1) For single-track deposited layer, the effect of wire feeding mode on the size and shape of deposited layer is greater than that of wire feeding angle.

(2) The variation of wire feeding mode changes the position of wire feeding into molten pool, affects the flow of wire molten